

## The Two-Point Correlation Function at Redshift $1/3$

C. W. Shepherd<sup>1</sup> R. G. Carlberg<sup>1,2</sup> H. K. C. Yee<sup>1,2</sup>

and

E. Ellingson<sup>2,3</sup>

### ABSTRACT

We present the results of a study of the two-point correlation function for a sample of field galaxies taken from the CNOC cluster survey. The sample consists of 144 galaxies within a contiguous region of space subtending 225 square arcminutes. The objects have  $r$ -band magnitudes  $17.0 \leq r \leq 21.7$  and redshifts  $0.21 \leq z \leq 0.53$ . The median redshift of the sample is  $\bar{z} = 0.36$ . The real space correlation function is found to be consistent with a power law  $\xi(r) = (r/r_0)^{-1.7}$  with  $r_0 = 2.1_{-0.3}^{+0.6} h^{-1}\text{Mpc}$  ( $\Omega_0 = 1$ ), or  $r_0 = 2.5_{-0.4}^{+0.7} h^{-1}\text{Mpc}$  ( $\Omega_0 = 0.2$ ). Uncertainties are estimated using the bias-corrected bootstrap resampling method, with 300 resamplings. This low correlation length implies strong evolution since  $z \sim 0.36$  has occurred in either the correlation function or the luminosity function; if the observed correlation function is modeled as  $\xi(r, z) = \xi(r, 0)(1 + z)^{-(3+\varepsilon)}$  with  $\xi(r, 0) = (r/5.1 h^{-1}\text{Mpc})^{-1.7}$ , then  $\varepsilon = 0.8_{-1.3}^{+1.0}$ . Comparison of the redshift space and real space correlation function indicates that the one-dimensional pairwise peculiar velocity dispersion  $\sigma$  at  $z \approx 0.36$  is weakly inconsistent with  $770 \text{ km s}^{-1}$ , the value predicted by the Cosmic Virial Theorem if  $\Omega_0 = 1$ . The observed correlation function is, however, consistent with  $\sigma = 400 \text{ km s}^{-1}$ , the value expected if  $\Omega_0 = 0.2$ .

*Subject headings:* large-scale structure of the universe — galaxies: clustering  
— galaxies: evolution

---

<sup>1</sup>Department of Astronomy, University of Toronto, Toronto, Ont., Canada M5S 3H8

<sup>2</sup>Guest observer, Canada-France-Hawaii Telescope, operated jointly by NRC of Canada, CNRS of France, and the University of Hawaii

<sup>3</sup>C.A.S.A., University of Colorado, Campus Box 389, Boulder, CO 80309-0389

## 1. Introduction

The study of the statistics of galaxy clustering has yielded important information about the large-scale structure of the universe and about the environment of galaxies. One of the most useful statistics employed in this study is the two-point correlation function. This statistic quantifies the clustering of galaxies, and is directly related to the power spectrum of density fluctuations in the galaxy distribution. Determining the evolution of the correlation function is therefore essential for an understanding of cosmological structure formation.

The two-point correlation function has been extensively studied at low redshifts; Efstathiou (1995) gives a summary of redshift surveys that have been used for correlation analysis. Observations of the correlation function at the present epoch indicate that it is well described by a power law

$$\xi(r) = \left(\frac{r}{r_0}\right)^{-\gamma} \quad (1)$$

at scales  $r \lesssim 10 h^{-1}\text{Mpc}$ . Here, and throughout this paper, all separations are given in physical, as opposed to comoving, coordinates unless otherwise stated; the Hubble parameter is taken to be  $H_0 = 100h \text{ km s}^{-1}\text{Mpc}^{-1}$ . Typical results from optical surveys of nearby galaxies include  $r_0 = 5.4 \pm 0.3 h^{-1}\text{Mpc}$ ,  $\gamma = 1.77 \pm 0.04$  from the Center for Astrophysics (CfA) survey (Davis & Peebles 1983) and  $r_0 = 5.1 \pm 0.2 h^{-1}\text{Mpc}$ ,  $\gamma = 1.71 \pm 0.05$  from the Stromlo-APM survey (Loveday et al. 1995). Values for  $r_0$  and  $\gamma$  for local samples are typically taken to be  $5.4 h^{-1}\text{Mpc}$  and 1.8, respectively, based on the CfA observations. For the purposes of comparing our results to those from local samples, however, we adopt  $r_0 = 5.1 h^{-1}\text{Mpc}$  and  $\gamma = 1.7$ , principally because of the fainter magnitude limits used in the Stromlo-APM survey.

The principal aim of this investigation is to examine the evolution of the correlation function. A useful empirical model for this evolution, introduced by Koo & Szalay (1984) is

$$\xi(r, z) = \xi(r, 0) (1 + z)^{-(3+\varepsilon)} . \quad (2)$$

In this model,  $\varepsilon = \gamma - 3$  corresponds to clustering fixed in comoving coordinates, as seen in biased Cold Dark Matter (CDM) simulations (Carlberg 1991). If  $\varepsilon = 0$ , clustering is stable in physical coordinates. Colin & Carlberg (1996) find  $\varepsilon \sim 0$  for an Open CDM (OCDM) initial power spectrum with  $\Omega_0 = 0.2$ .

To determine  $\varepsilon$ , one must compute the correlation function from data from an earlier epoch. The most common method is to compute the angular correlation function from the angular galaxy distribution (e.g. Koo & Szalay 1984, Efstathiou et al. 1991 and Infante & Pritchet 1995). This method does not require that the distances to the objects in the

sample be known; rather, the clustering is observed as a two-dimensional projection of the three-dimensional clustering over a wide range of redshifts. In order to estimate the amount of clustering evolution present in the data, therefore, models for both the present-day correlation function and the redshift distribution of objects in the sample must be employed. Both Efstathiou et al. (1991) and Infante & Pritchett (1995) find  $\varepsilon > 0$  if  $\Omega_0 = 1$  and there is no evolution in the luminosity function.

In order to produce a reliable estimate of the spatial two-point correlation function, redshifts for a large number of objects must be obtained. Pencil-beam surveys using multi-object spectroscopy (MOS), such as the Autofib survey (Cole et al. 1994) and the Canada-France Redshift Survey (CFRS) (Le Fèvre et al. 1996) are the only surveys to date which contain a sufficient number of objects at intermediate redshifts. Le Fèvre et al. (1996) find  $\varepsilon \sim 0 - 2$  in the CFRS survey, consistent with the evolution observed in angular surveys.

In principle, data from pencil-beam surveys may be used to estimate the redshift space correlation function. The required velocity accuracy is, however, quite high. Davis & Peebles (1983) find the one-dimensional pairwise peculiar velocity dispersion in the CfA survey to be  $\sigma = 340 \pm 40 \text{ km s}^{-1}$  at a separation of  $1 h^{-1}\text{Mpc}$ . If the velocity errors in a survey are comparable to  $\sigma/\sqrt{2}$ , computation of a reliable redshift space correlation function from that survey is impossible. Cole et al. (1994) find a comoving correlation length  $r_0 = 6.5 \pm 0.4 h^{-1}\text{Mpc}$  based on the redshift space correlation function for the Autofib survey. The median redshift of this survey is  $\bar{z} = 0.16$ ; taking  $r_0(0.16) = 6.5/1.16 h^{-1}\text{Mpc}$  and  $r_0(0) = 5.1 h^{-1}\text{Mpc}$  in equation (2) yields  $\varepsilon \approx -4$ , at odds with previous angular correlation results.

We present here estimates of the real space and redshift space two-point correlation function for a sample of field galaxies taken from the Canadian Network for Observational Cosmology (CNOC) cluster survey. The data are described in Section 2. The techniques used for computing the real space two-point correlation function and its evolution, along with the results for this survey, are presented in Section 3. Also described there is our investigation of the redshift space two-point correlation function and the heretofore unknown pairwise peculiar velocity dispersion at  $z \sim 0.36$ . Our conclusions are given in Section 4.

## 2. Data

The data used here are taken from the CNOC cluster survey. The observational procedures and data reduction are described in detail in Yee, Ellingson & Carlberg (1996); only the relevant features of the survey are discussed here. The data were obtained using the multi-object spectrograph (MOS) at the Canada-France-Hawaii Telescope (CFHT). A band-limiting filter was used with the spectrograph to reduce the length of each spectrum, further increasing the multiplexing rate. Since the CNOC survey is a cluster redshift survey, each field was chosen to contain a cluster at its center – most of the data is therefore unsuitable for investigating the clustering of field galaxies. One field in the survey, MS1512+36, however, is well suited to a correlation analysis of field galaxies, since the cluster is quite poor. Only data from this field are analyzed here; the complete data set is described and presented in Abraham et al. (1996).

Pencil-beam surveys present several problems related to the fairness of the sample (a sample is said to be fair if the structure contained within it is representative of the global average). The first difficulty relates to the beam width; a typical beam diameter of  $10'$  yields a width of  $\sim 1.8 h^{-1}\text{Mpc}$  at  $z = 1/3$  ( $\Omega_0 = 1$ ), the same order of magnitude as the expected correlation length  $r_0$  at that redshift, given any reasonable amount of evolution in the correlation function.

Thus, the distribution of objects in a beam may be dominated by a single large density inhomogeneity, biasing the estimation of  $\xi$ . One possible solution to this problem is to calculate the correlation function from data taken from many pencil-beams scattered randomly throughout the sky. This approach does not make optimal use of the data, however; it is preferable to place the beams so that the beam-beam separation is comparable to the beam width, thus increasing the number of pairs of objects with separations  $\sim r_0$ . The MS1512+36 data are from a mosaic of three fields from the survey, with a total angular size of  $27' \times 8'$  (222 square arcminutes). Despite the relatively large width of the sample ( $4.9 h^{-1}\text{Mpc}$  at  $z = 0.36$  if  $\Omega_0 = 1$ ), there remains a large overdensity spanning the width of the field. The effect of this inhomogeneity is discussed below.

A second, more subtle, problem with MOS data is that of selection effects. Magnitude selection may bias the sample towards bright objects, which will lead to erroneous results if bright objects cluster differently from faint objects. More importantly, MOS produces a lower limit on the separation of objects for which spectra may be observed. Once one object is designated to be observed through a slit on a given mask, the placement of the spectra on the detector precludes designing another slit closely above or below the first. This results in high density regions being sampled less completely than low density regions, thereby reducing the observed correlation. Each of the three fields composing the MS1512+36 data

was observed with 2 different MOS masks, with a higher priority given in the second mask to completing observations of closely spaced pairs (see Yee et al. 1996 for details). This somewhat reduces the amount of geometric selection.

To correct for the magnitude and geometric selection, the magnitude weight  $w_m$  and local magnitude weight  $w_{lm}$  are calculated from the data for each object in the sample. For a given object with apparent magnitude in the bin  $(m, m + \Delta m)$  and observed redshift  $z$ ,  $w_m$  is proportional to the fraction of objects anywhere in the sample in the same magnitude bin which have observed redshifts. The local magnitude weight  $w_{lm}$  for an object is proportional to the fraction of objects in a circle with radius  $120''$  about the first object in the same magnitude bin which have observed redshifts. Also defined for each object is the geometric weight  $w_{xy} = w_{lm}/w_m$ , which is related to the number of nearby objects at any magnitude which have observed redshifts. A detailed explanation of the weighting procedure is given in Yee et al. (1996); a test of the extent to which these weights correct for the sampling nonuniformities is described in Section 3.1.

Three subsamples of the MS1512+36 data are created; the photometric, redshift and field samples. The photometric sample, used for computing the angular correlation function, consists of the 404 objects with  $g - r$  colours, with Gunn  $r$ -band magnitude in the range  $17.0 \leq r \leq 21.7$ . The upper limit is chosen so that the magnitude weight of every object in the redshift sample is less than 5; the lower limit is employed since the masks were designed to exclude objects much brighter than the brightest cluster galaxy, which has  $r = 18.45$ .

The redshift sample consists of all objects in the photometric sample which have identified redshifts in the range  $0.21 \leq z \leq 0.53$ . These limits are chosen so that the spectral features used to identify emission line objects lie within the optimal response region of the filter. This sample is shown in Figure 1. The use of band-limiting filters for the CNOC survey results in strong redshift selection effects in the sample, which are easily understood by noting the visibility of strong spectral features in our limited spectral window. In this analysis we have extended the lower  $z$  limit from 0.27 in Yee, Ellingson & Carlberg (1996) to 0.21. The original higher limit was based on the detection of [O II]  $\lambda 3727$  at the blue end of the spectrum. However, the wavelength limits for the filter used are such that as [O II]  $\lambda 3727$  disappears at the blue end, the [O III]  $\lambda\lambda 4959, 5007$  lines come in on the red end. From our sample, we have found that whenever the [O III]  $\lambda\lambda 4959, 5007$  and [O II]  $\lambda 3727$  lines are both within the spectral range, they are always detected simultaneously. Hence we can safely use the [O III]  $\lambda\lambda 4959, 5007$  lines to extend our lower redshift limit; no significant selection bias as a function of spectral type is seen in the redshift sample (Yee et al. 1996).

The field sample is constructed from the redshift sample by removing the 38 objects that have redshifts  $0.3656 \leq z \leq 0.3796$ . This redshift range corresponds to a velocity range

of  $\pm 2100 \text{ km s}^{-1}$ , or six times the velocity dispersion of the cluster, at  $z = 0.3727$ , the center of the cluster (Carlberg et al. 1996). The field sample therefore almost certainly excludes all cluster members, thus removing the bias towards high density regions present in the redshift sample. The field sample contains 144 objects, with a median redshift of  $\bar{z} = 0.36$ .

As can be seen in Figure 1, the cluster appears to be embedded in an overdensity extending across the field. In order to test the sensitivity of our results to the presence of this structure, we have computed the correlation functions for the field sample with all objects with  $0.354 \leq z \leq 0.390$  removed. The results are consistent with those computed from the entire field sample, although, as there are only 118 objects in the field sample outside the these extended redshift limits, the uncertainties are considerably larger. We conclude that the presence of this structure does not unduly influence our results.

### 3. Analysis

#### 3.1. Estimating the Correlation Function

The two-point correlation function  $\xi$  is defined by (Peebles, 1980)

$$\delta P(r) = \bar{n} (1 + \xi(r)) \delta V, \quad (3)$$

where  $\delta P(r)$  is the probability of finding a second object in a volume  $\delta V$  with a physical separation  $r$  from a randomly chosen object, and  $\bar{n}$  is the mean density of objects. For a finite sample of objects, and some (small) fixed separation difference  $\Delta r$ ,  $\xi(r)$  may be estimated from equation (3) as

$$1 + \xi(r) \approx \frac{DD(r)}{N_D^2} \frac{V}{\Delta V(r)}. \quad (4)$$

Here,  $N_D$  is the number of objects in the sample,  $DD(r)$  is the number of ordered pairs of objects in the sample with separation between  $r$  and  $r + \Delta r$ ,  $V$  is the volume of the sample, and  $\Delta V(r)$  is the average volume of the set surrounding a first object in which a second may be found with separation between  $r$  and  $r + \Delta r$  from the first.

The volumes  $\Delta V$  in equation (4) may be arbitrarily complicated; in practice, they are estimated using Monte-Carlo integration. A random data set containing  $N_R$  objects is generated within the volume of the original data set in a manner such that the random catalog is subject to the same selection criteria as the data. If the number of pairs of objects with separation between  $r$  and  $r + \Delta r$ , the first object belonging to the data set, the second

to the random set, is  $DR(r)$ , then (Davis & Peebles 1983)

$$1 + \xi(r) \approx \frac{N_R}{N_D} \frac{DD(r)}{DR(r)}. \quad (5)$$

The pair counts  $DD$  and  $DR$  in equation (5) may be computed with arbitrary weights, so that  $DD(r) = \sum_{i,j} w_i^{(D)} w_j^{(D)}$  and  $DR(r) = \sum_{i,j} w_i^{(D)} w_j^{(R)}$ , where the sums are taken over all data-data or data-random pairs of objects with separation between  $r$  and  $r + \Delta r$ , respectively, and  $w_i^{(D)}$  and  $w_i^{(R)}$  are the weights to be applied to  $i$ 'th data and random object, respectively. The object counts  $N_D$  and  $N_R$  in equation (5) are replaced with the weighted object counts  $D = \sum_{i=1}^{N_D} w_i^{(D)}$  and  $R = \sum_{i=1}^{N_R} w_i^{(R)}$ , respectively. The correlation function is then estimated as

$$1 + \xi(r) \approx \frac{R}{D} \frac{DD(r)}{DR(r)}. \quad (6)$$

To correct for the selection effects present in this sample, and for the incompleteness present in any magnitude-limited sample, we take the total weight for an object at redshift  $z$  with local magnitude weight  $w_{lm}$  to be  $w_{tot} = w_{lm}/\phi(z)$ , where  $\phi(z)$  is the redshift selection function, defined as the fraction of objects at redshift  $z$  which lie within the apparent magnitude limits of the survey. These total weights are then used for computing the pair and object counts defined above.

The selected random catalog is generated by first creating a uniform random catalog, by randomly distributing objects throughout the sample volume in such a way that the comoving density of objects is constant. Apparent magnitudes are then assigned to each object in the uniform random catalog using the process described below, and those objects lying outside the magnitude limits of the survey are discarded. Finally, the local magnitude selection is estimated at the position of each object random object, and objects failing the selection criteria are discarded. For small data sets, this method is preferable to smoothing the observed redshift distribution, since the redshift distribution is dominated by density inhomogeneities comparable to the width of the sample, making the random distribution obtained sensitive to the smoothing window used.

Absolute magnitudes for the objects in the field sample are required to determine the luminosity function, which is used for generating the absolute magnitudes for the random objects. The K-corrections are obtained by interpolating from model K-corrections in the  $r$  and  $g$  bands as a function of redshift for non-evolving galaxies of 4 spectral types (E+S0, Sbc, Scd, and Im). The models are derived by convolving filter response functions with spectral energy distributions in Coleman, Wu, & Weedman (1980). These values are then corrected from the AB system to the standard Gunn system (Thuan & Gunn 1976). For each galaxy with redshift, a spectral classification is estimated by comparing the observed

$g - r$  color with the model colors at the same redshift. The spectral classification, obtained via interpolation, is treated as a continuous variable between the 4 spectral types. From the spectral classification, the appropriate K-correction to the  $r$  magnitude is then derived using the models.

The  $r$ -band absolute magnitudes for the random catalog are generated according to the luminosity function for the data. The luminosity function is modeled as a non-evolving Schechter function (Schechter, 1976)

$$\Phi(M_r) = 0.4 \ln 10 \phi^* 10^{0.4(1+\alpha)(M_r^* - M_r)} \exp\left(-10^{0.4(M_r^* - M_r)}\right), \quad (7)$$

where  $\Phi(M_r)$  is the comoving number density of objects with absolute magnitude  $M_r$  per unit magnitude. The assumption of no evolution is reasonable, since the redshift range of the field sample is relatively small. The parameters  $M_r^*$  and  $\alpha$  are adjusted to fit the data using a least-squares fit. The luminosity function (after an appropriate renormalization, which removes the dependence on  $\phi^*$ ) is then used as the probability distribution for the absolute magnitudes of the objects in the uniform random catalog. An intrinsic colour  $(g - r)_0$  is then chosen for each object, in a manner such that the distribution of intrinsic colours in the uniform random catalog is the same as that in the data catalog. The  $r$ -band absolute magnitude  $M_r$  and intrinsic colour  $(g - r)_0$  for each object are then used to compute the K-corrections, using the method described in Section 2.

For each object in the uniform random catalog with apparent magnitude within the sample limits, magnitude and geometric weights  $w_m$  and  $w_{xy}$  are estimated by interpolating from the data weights. The magnitude weight interpolation is a straightforward one-dimensional interpolation. The two-dimensional geometric weight interpolation is performed by convolving the spatial map of geometric weights of each data object with a Gaussian with dispersion  $\sigma = 1'$ . The values of the convolved weights at the position of the random object are then summed, yielding a weight for that random object. The local magnitude weight  $w_{lm}$  for the random object is then calculated from  $w_m$  and  $w_{xy}$ ; the object is discarded unless  $1/w_{lm}$  is less than a randomly chosen number between 0 and 1. The redshift selection function  $\phi(z)$  is then computed from the luminosity function parameters  $M_r^*$  and  $\alpha$  and the sample magnitude limits;  $w_{lm}$  and  $\phi(z)$  are then combined to give a total weight  $w_{tot} = w_{lm}/\phi(z)$  for each remaining object in the selected random catalog.

The redshift distribution for a random catalog generated in this manner is compared to the redshift distribution of the redshift sample in Figure 2. The random distribution has been rescaled to have the same number of objects within the redshift sample redshift range as the data distribution in this figure. Note that the random distribution is much more uniform than the distribution that would be obtained by smoothing the data distribution, due to the presence of the large structure discussed earlier.

This method of generating the random catalog and the weighting procedure are tested by comparing the angular correlation functions of the photometric and redshift samples. The angular correlation function  $w$  is estimated in a manner similar to that given in equation (6);

$$1 + w(\theta) \approx \frac{R}{D} \frac{DD(\theta)}{DR(\theta)}, \quad (8)$$

where the pair counts are now taken over pairs with angular separation  $\theta$ . If the model (1) for  $\xi$  is correct, then (Peebles 1980)

$$w(\theta) = A_w \left( \frac{\theta}{1''} \right)^{-\delta}, \quad (9)$$

where  $\delta = \gamma - 1$ .

The random catalog used for computing  $w$  for the redshift sample is generated using the procedure described above, while the catalog for the photometric sample was generated uniformly; both catalogs contain 10 000 objects. Figure 3 shows the results of a power-law fit to the angular correlation for the photometric sample, with  $\delta$  fixed to 0.7, and  $w$  for the redshift sample. The amplitudes in equation (9) are found to be  $A_w = 1.3_{-0.1}^{+0.4}$  for the photometric sample, and  $A_w = 1.2_{-0.0}^{+1.2}$  for the redshift sample. The consistency of these amplitudes indicates that the total weights adequately describe the selection effects present in the data. The photometric sample value of  $A_w$  implies  $w(1') \approx 0.07$ , consistent with the value found by Infante & Pritchet (1995) for a sample of objects with  $F \leq 22$ . The uncertainties in all correlations and fitted parameters given here are the 68.3% confidence intervals computed using the bias-corrected bootstrap resampling method, described by Efron & Tibshirani (1986). Three hundred resamplings are used for each computation, the minimum recommended for this method.

### 3.2. The Real Space Correlation Function

Two different correlation functions are derivable from redshift data; the redshift space correlation function  $\xi(s)$  and the real space function  $\xi(r)$ . If the separation of a pair of objects is computed directly from redshifts, it includes the line-of-sight component of the object's peculiar velocities relative to the Hubble flow. For the range of separations of interest here, the random internal motions of bound groups of objects dominate, elongating structures along the line of sight. This elongation reduces the observed correlation at small separations, so the power-law model (1) is expected to be valid only for the real space correlation function.

### 3.2.1. Method

Although it is impossible to measure real space separations directly using only redshift data, it is possible to estimate the parameters of a model for the real space correlation function. This is accomplished by decomposing the redshift space separation of a pair of objects into components parallel and perpendicular to the line of sight to the pair. Since the redshift space distortions act only along the line of sight, functions of the perpendicular component must be independent of these perturbations.

The decomposition is performed assuming the separations are small, so that the effects of curvature may be neglected. Thus, given two objects with redshifts  $z_1$  and  $z_2$  and angular separation  $\theta_{12}$ , two vectors  $\mathbf{x}_i$  ( $i = 1, 2$ ) are formed, such that

$$|\mathbf{x}_i| = \frac{2c}{H_0} \frac{\Omega_0 z - (2 - \Omega_0)(\sqrt{1 + \Omega_0 z} - 1)}{\Omega_0^2(1 + z)} \quad (i = 1, 2) \quad (10)$$

( $\Lambda = 0$ ), and

$$\mathbf{x}_1 \cdot \mathbf{x}_2 = |\mathbf{x}_1| |\mathbf{x}_2| \cos \theta_{12} . \quad (11)$$

The comoving redshift space separation of the pair is then  $\mathbf{s} \approx \mathbf{x}_2 - \mathbf{x}_1$ , and the line of sight to the pair is  $\bar{\mathbf{x}} = \frac{1}{2}(\mathbf{x}_1 + \mathbf{x}_2)$ . The components of the physical separation parallel and perpendicular to the line of sight are then

$$\pi = \frac{\mathbf{s} \cdot \bar{\mathbf{x}}}{(1 + \bar{z}) |\bar{\mathbf{x}}|} \quad (12)$$

and

$$r_p = \frac{\sqrt{|\mathbf{s}|^2 - \pi^2}}{1 + \bar{z}} , \quad (13)$$

where  $\bar{z} = \frac{1}{2}(z_1 + z_2)$ . The definition of the correlation function (3) is then generalized to describe the probability in excess of random of finding an object with redshift space separation  $(r_p, \pi)$  from a randomly chosen object. This is estimated as

$$1 + \xi(r_p, \pi) \approx \frac{R}{D} \frac{DD(r_p, \pi)}{DR(r_p, \pi)} , \quad (14)$$

where  $DD(r_p, \pi)$  and  $DR(r_p, \pi)$  are the weighted number of data-data and data-random ordered pairs with separations  $(r_p, \pi)$ , respectively, and  $D$  and  $R$  are the weighted object counts defined in section 3.1.

Although  $\xi(r_p, \pi)$  is affected by the redshift space distortions described earlier, the projected correlation function  $w_p(r_p)$ , defined by

$$w_p(r_p) = \int_{-\infty}^{\infty} \xi(r_p, \pi) d\pi \quad (15)$$

is not. Thus,

$$w_p(r_p) = \int_{-\infty}^{\infty} \xi(\sqrt{r_p^2 + x^2}) dx , \quad (16)$$

where the integral is over the real space correlation function. If the power law model (1) is employed, then (Davis & Peebles 1983)

$$w_p(r_p) = \sqrt{\pi} \frac{\Gamma\left(\frac{\delta}{2}\right)}{\Gamma\left(\frac{\delta-1}{2}\right)} r_0 \left(\frac{r_p}{r_0}\right)^{-\delta} . \quad (17)$$

The integral in equation (15) must be truncated at some  $\pi_{max}$  for any real data set. Figure 4 shows the quantity  $2\pi\bar{n}J_p(1 h^{-1}\text{Mpc}, \pi)$  vs  $\pi$  for the field sample, where

$$J_p(r_p, \pi) = \int_{-\pi}^{\pi} \int_0^{r_p} \xi(r'_p, \pi') r'_p dr'_p d\pi' . \quad (18)$$

Given this definition, the quantity  $2\pi\bar{n}J_p(r_p, \pi)$  represents the mean number of objects in excess of random within the cylinder with radius  $r_p$  and length  $2\pi$  centered on an object in the sample. This function is expected to increase with  $\pi$  for small  $\pi$ , approaching some limiting value. As can be seen, cutoffs less than  $\sim 3 h^{-1}\text{Mpc}$  exclude real power in  $\xi(r_p, \pi)$ , while noise appears to be the primary contributor to the integral (18) for  $\pi \gtrsim 50 h^{-1}\text{Mpc}$ . We adopt  $15 h^{-1}\text{Mpc}$  as the cutoff to be used in equation (15); no significant change in the derived correlation length is observed when the cutoff is varied between  $5 h^{-1}\text{Mpc}$  and  $35 h^{-1}\text{Mpc}$ .

### 3.2.2. Results

The projected correlation function  $w_p(r_p)$  is calculated for the field sample using equation (14), with the integral truncated at  $15 h^{-1}\text{Mpc}$ . The random catalog is generated using the method described in Section 3.1; the catalog contains 200 000 objects with redshifts. The pair counts  $DD$  and  $DR$  and object counts  $D$  and  $R$  are calculated using the total weights defined in section 3.1. The results are shown in Figure 5;  $r_0$  is determined for  $\Omega_0 = 1$  and 0.2 by fitting the model (17) to the data with  $\delta$  fixed to 0.7. The correlation length is found to be  $r_0 = 2.1_{-0.3}^{+0.6} h^{-1}\text{Mpc}$  ( $\Omega_0 = 1$ ) or  $r_0 = 2.5_{-0.4}^{+0.7} h^{-1}\text{Mpc}$  ( $\Omega_0 = 0.2$ ), considerably smaller than the values found locally.

If it is assumed that the population in our sample at  $z \sim 0.36$  will evolve to the population observed at  $z = 0$  in optical surveys, equation (2) may be used, with  $r_0(0)$  equal to the value observed in the local sample, to estimate  $\varepsilon$ . Applying equation (2), with  $r_0 = 2.1_{-0.3}^{+0.6} h^{-1}\text{Mpc}$  at  $z = 0.36$  and  $r_0 = 5.1 h^{-1}\text{Mpc}$  at  $z = 0$  yields  $\varepsilon = 1.8_{-1.5}^{+0.9}$  ( $\Omega_0 = 1$ );

using  $r_0 = 2.5_{-0.4}^{+0.7} h^{-1}\text{Mpc}$  gives  $\varepsilon = 0.8_{-1.3}^{+1.0}$  ( $\Omega_0 = 0.2$ ). Thus, the correlation is found to be increasing with redshift in physical coordinates, although the  $\Omega_0 = 0.2$  estimate of  $\varepsilon$  is consistent with no evolution. Correlation fixed in comoving coordinates ( $\varepsilon = 3 - \gamma$ ) is effectively ruled out.

An alternate explanation for the low correlation length is that some of the objects in our sample are weakly clustered and become intrinsically faint at the present epoch (Efstathiou et al. 1991). That is, the evolution is in the luminosity function, not the correlation function. This is entirely feasible in our sample; if  $r_0 = 5.1 h^{-1}\text{Mpc}$  locally, and  $r_0 = 2.5 h^{-1}\text{Mpc}$  at  $z = 0.36$ , and  $\varepsilon = 0$ , and the faint population is completely unclustered ( $\xi = 0$ ), then the fraction of objects in our sample which belong to this currently faint population is only  $\sim 0.15$ . If the faint population is clustered realistically, say  $r_0 = 3.8 h^{-1}\text{Mpc}$  (as seen in the IRAS survey, Fisher et al. 1994a) for both the faint galaxy autocorrelation and faint-bright cross-correlation, then  $\sim 40\%$  of the objects in our sample are required to be undetected in the present-epoch observations. Thus, we cannot rule out evolution in the luminosity function as the source of the reduction in  $r_0$  at intermediate redshifts.

### 3.3. The Redshift Space Correlation Function

As noted in section 3.2, the redshift space correlation function is not expected to be a power-law due to random peculiar velocities. However, measurements of  $\xi(s)$  can be used, in conjunction with a model for the real space correlation function, to provide information about the velocity distribution of objects in the sample. This in turn yields information on the mean matter density.

#### 3.3.1. Method

The real space correlation function  $\xi(r)$  is related to  $\xi(r_p, \pi)$  by (Peebles 1980)

$$1 + \xi(r_p, \pi) = \int g(r, \mathbf{v}) (1 + \xi(r)) d^3v, \quad (19)$$

where  $g(r, \mathbf{v})$  is the distribution of relative peculiar pairwise velocities of pairs with separation  $r$ , and  $r^2 = r_p^2 + (\pi - v_z/H(z))^2$ , where  $v_z$  is the component of  $\mathbf{v}$  along the line of sight. To obtain a relation between the redshift space correlation function  $\xi(s)$  and the real space correlation function  $\xi(r)$ , one integrates equation (19) over a sphere of radius  $s$ ;

$$4\pi \int_{-s}^s \xi(s') s'^2 ds' = 2\pi \int \int_{-s}^s \int_0^{\sqrt{s^2 - \pi^2}} \xi(r) g(r, \mathbf{v}) r_r dr_p d\pi d^3v, \quad (20)$$

using the identity  $2\pi \int_{-s}^s \int_0^{\sqrt{s^2-\pi^2}} \xi(r_p, \pi) r_p dr_p d\pi = 4\pi \int_0^s \xi(s') s'^2 ds'$ .

We employ here a simplified model for the pairwise peculiar velocity distribution in which  $g$  is independent of the separation  $r$ . Two dimensions of the velocity integral in equation (20) may therefore be performed immediately; we define the line-of-sight peculiar pairwise velocity distribution  $f(v_z) = \int_{-\infty}^{\infty} \int_{-\infty}^{\infty} g(v_x, v_y, v_z) dv_x dv_y$ . Equations(20) then reduces to

$$4\pi \int_0^s \xi(s') s'^2 ds' = 2\pi \int_{-\infty}^{\infty} \int_{-s}^s \int_0^{\sqrt{s^2-\pi^2}} \xi(r) f(v_z) r_p dr_p d\pi dv_z, \quad (21)$$

where the integral on the left is over the redshift space correlation function, while the integral on the right is over the real space correlation function. Differentiating equation (21) with respect to  $s$  gives the general relationship between the redshift space and real space correlation functions, under the assumption that  $g$  is independent of  $r$ ;

$$\xi(s) = \frac{1}{2} s^{-1} \int_{-\infty}^{\infty} \int_{-s}^s \xi \left( \sqrt{s^2 - 2(v_z/H(z))\pi + (v_z/H(z))^2} \right) f(v_z) d\pi dv_z. \quad (22)$$

The argument to the real space correlation function in equation (22) is just the physical separation  $r$ , evaluated with  $r_p = \sqrt{s^2 - \pi^2}$ . If  $\xi(r)$  is modeled as a power law (1), then the integral over  $\pi$  in equation (22) may be performed analytically, finally yielding

$$\xi(s) = \frac{1}{2(2-\gamma)} H(z) r_0^\gamma s^{-1} \int_{-\infty}^{\infty} \left( |s + v_z/H(z)|^{2-\gamma} - |s - v_z/H(z)|^{2-\gamma} \right) f(v_z) \frac{dv_z}{v_z}. \quad (23)$$

The simplified model for the velocity distribution used here takes  $f$  to be an exponential with zero mean, and dispersion independent of separation;

$$f(v_z) = \sqrt{\frac{1}{2\sigma^2}} \exp \left( -\sqrt{2} \left| \frac{v_z}{\sigma} \right| \right). \quad (24)$$

Here,  $\sigma^2$  is the projected pairwise peculiar velocity dispersion; the three-dimensional mean-square pairwise peculiar velocity  $\langle v^2 \rangle = 3\sigma^2$ , since the mean pairwise peculiar velocity is taken to be zero.

Given a value for the cosmological density parameter  $\Omega_0$ ,  $\sigma$  may be estimated using the Cosmic Virial Theorem (Peebles 1980, Fisher et al. 1994b);

$$\sigma^2(r, z) = \frac{3H(z)^2 \Omega(z) Q J r_0(z)^\gamma r^{2-\gamma}}{4b(\gamma-1)(2-\gamma)(4-\gamma)}, \quad (25)$$

where  $Q$  relates the two- and three-point correlation functions,  $b$  is the linear bias factor and  $J$  depends only on  $\gamma$  ( $J(\gamma = 1.7) = 4.14$ ). For  $\gamma$  close to 2,  $\sigma$  is almost independent of separation, consistent with equation (24). Equation (25) depends on the relation between the distributions of galaxies and matter through the (unknown) bias factor, and thus is of limited use as a probe of the true value of  $\Omega_0$ . Note that according to this model,  $\sigma$  evolves as  $(1+z)^{-\epsilon/2}$  (holding  $\gamma$  and  $Q$  constant).

### 3.3.2. Results

The redshift space correlation function is calculated for the field sample using the redshift space analogue of equation (6)

$$1 + \xi(s) \approx \frac{R}{D} \frac{DD(s)}{DR(s)}, \quad (26)$$

where  $DD(s)$  and  $DR(s)$  are the number of data-data and data-random pairs with redshift space separations between  $s$  and  $s + \Delta s$ , respectively. The random catalog used here is the same as that used for computing the real space correlation function. Figure 6 shows  $\xi(s)$  for the field sample, along with the predictions from equation (23), using  $r_0 = 2.1 h^{-1}\text{Mpc}$ ,  $\gamma = 1.7$  and  $\sigma = 770 \text{ km s}^{-1}$  for  $\Omega_0 = 1$ , and  $r_0 = 2.5 h^{-1}\text{Mpc}$ ,  $\gamma = 1.7$  and  $\sigma = 400 \text{ km s}^{-1}$  for  $\Omega_0 = 0.2$ . These values of  $\sigma$  are computed using equation (25) with  $Q = b = 1$ . Also shown are the curves given by equation (23) using a Gaussian pairwise peculiar velocity distribution with  $\sigma = 140 \text{ km s}^{-1}$ ; this value corresponds to the mean velocity uncertainty in the sample of  $100 \text{ km s}^{-1}$ .

As can be seen, the  $\sigma = 770 \text{ km s}^{-1}$ ,  $\Omega_0 = 1$  model overestimates the redshift space perturbations. A least-squares fit of equation (23) to the data, using equations (24) and (25), with  $\Omega_0 = 1$ ,  $b = 1$  and  $\gamma = 1.7$  yields  $r_0 = 3.9_{-0.6}^{+0.7} h^{-1}\text{Mpc}$ , inconsistent with the value derived from the projected correlation function data,  $r_0 = 2.1_{-0.3}^{+0.6} h^{-1}\text{Mpc}$ , with 90% confidence. The  $\sigma = 400 \text{ km s}^{-1}$ ,  $\Omega_0 = 0.2$  model matches the data more closely, consistent with the low  $\Omega_0$  favored by Davis & Peebles (1983) and Fisher et al. (1994b). However, the observed  $\xi(s)$  is consistent with a model with zero pairwise peculiar velocity dispersion, and the redshift space distortions due solely to velocity measurement errors; more data are therefore needed for a precise determination of  $\sigma$ . We conclude that the data are best modeled by a low density parameter; taking  $\Omega_0 = 0.2$ ,  $r_0 = 2.5_{-0.4}^{+0.7} h^{-1}\text{Mpc}$  and  $\sigma = 400 \text{ km s}^{-1}$  yields models which are consistent with both the observed  $w_p(r_p)$  and  $\xi(s)$ .

## 4. Conclusions

We have found that the physical correlation length for  $0.21 \leq z \leq 0.53$  is  $r_0 = 2.1_{-0.3}^{+0.6} h^{-1}\text{Mpc}$  if  $\Omega_0 = 1$ , implying  $\varepsilon = 1.8_{-1.5}^{+0.9}$ . If  $\Omega_0 = 0.2$ ,  $r_0 = 2.5_{-0.4}^{+0.7} h^{-1}\text{Mpc}$  and  $\varepsilon = 0.8_{-1.3}^{+1.0}$ ; the uncertainties are estimated using the bias-corrected bootstrap resampling method, with 300 resamplings. These results are consistent with earlier results obtained from angular surveys, which indicate rapid evolution (Efstathiou et al. 1991, Infante & Pritchett 1995). It is also consistent with the results from the CFRS (Le Fèvre et al. 1996). This decrease in  $r_0$  from its present value may be interpreted either as a real change in the

clustering of the observed galaxies, or as due to a weakly clustered population at  $z \sim 0.36$  which is intrinsically faint at the present epoch.

The projected pairwise peculiar velocity dispersion at  $z = 0.36$ ,  $\sigma = 770 \text{ km s}^{-1}$ , predicted by the Cosmic Virial Theorem using  $\Omega_0 = 1$  is inconsistent at the 90% confidence level with the observed redshift space correlation function. The  $\Omega_0 = 1$  is therefore weakly rejected. The  $\Omega_0 = 0.2$  prediction,  $\sigma = 400 \text{ km s}^{-1}$ , however, matches the data more closely. Thus, the relatively small redshift space distortions present favour low  $\Omega_0$  as determined from the Cosmic Virial Theorem, consistent with the results of Davis & Peebles (1983) and Fisher et al. (1994b).

More data is required to obtain a precise value for  $\sigma$ , and larger scales need to be sampled in order to obtain a smooth redshift distribution, thereby removing uncertainties in  $\xi$  due to density inhomogeneities on the scale of the sample diameter. A larger sample would also enable computations of the correlation function for subsamples based on galaxy colour or intrinsic brightness, which would help distinguish between the two possible sources of observed evolution described in section 3.2. The CNOC2 redshift survey, presently in progress, will yield  $\sim 5000$  high-accuracy redshifts in the range  $0.15 \leq z \leq 0.7$ . This survey will contain enough objects, and sample sufficiently large scales, to permit accurate computations of the redshift space and real space correlation functions and their evolution at intermediate redshifts.

We thank all participants of the CNOC cluster survey for assistance in obtaining and reducing these data. The Canadian Time Assignment Committee for the CFHT generously allocated substantial grants of observing time, and the CFHT organization provided the technical support which made these observations feasible. We gratefully acknowledge financial support from NSERC and NRC of Canada.

## REFERENCES

- Abraham, R. G., Yee, H. K. C., Ellingson, E., Gravel, P., Carlberg, R. G., Smecker-Hane, T. A., & Pritchett, C. J. 1996, preprint
- Carlberg, R. G. 1991, *ApJ*, 367, 385
- Carlberg, R. G., Yee, H. K. C., Ellingson, E., Abraham, R., Gravel, P., Morris, S., & Pritchett, C. J. 1996, in press
- Cole, S., Ellis, R., Broadhurst, T., & Colless, M. 1994, *MNRAS*, 267, 541
- Coleman, G. D., Wu, C., & Weedman, D. W. 1980, *ApJS*, 43, 393

- Colin, P. & Carlberg, R. G. 1996, preprint
- Davis, M. & Peebles, P. J. E. 1983, *ApJ*, 267, 465
- Efron, B. & Tibshirani, R. 1986, *StatSci*, 1, 1, 54
- Efstathiou, G. 1988, in *Proc. 3rd IRAS Conf., Comets to Cosmology*, ed. A. Lawrence (New York: Springer), 312
- Efstathiou, G., Bernstein, G., Katz, N., Tyson, J. A., & Guhathakurta, P. 1991, *ApJ*, 380, L47
- Efstathiou, G. 1995, to appear in *Les Houches Lectures 1993* (Netherlands: Elsevier Science)
- Fisher, K. B., Davis, M., Strauss, M. A., Yahil, A., & Huchra, J. 1994a, *MNRAS*, 266, 50
- Fisher, K. B., Davis, M., Strauss, M. A., Yahil, A., & Huchra, J. P. 1994b, *MNRAS*, 267, 927
- Infante, L. & Pritchett, C. J. 1995, *ApJ*, 439, 565
- Koo, D. C. & Szalay, A. S. 1984, *ApJ*, 282, 390
- Le Fèvre, O., Hudon, D., Lilly, S. J., Crampton, D., Hammer, F., & Tresse, L. 1996, *ApJ*, in press
- Loveday, J., Maddox, S. J., Efstathiou, G., & Peterson, B. A. 1995, *ApJ*, 442, 457
- Peebles, P. J. E. 1980, *The Large-Scale Structure of the Universe* (Princeton: Princeton University Press)
- Schechter, P. 1976, *ApJ*, 203, 297
- Thuan, T. X. & Gunn, J. E. 1976, *PASP*, 88, 543
- Yee, H. K. C., Ellingson, E., & Carlberg, R. G. 1996, *ApJS*, in press

Fig. 1.— The MS1512+36 redshift sample. The angular scale has been expanded by a factor of  $\sim 80$ . The objects within the central box are not included in the field sample.

Fig. 2.— The redshift distribution  $\frac{dN}{dz}(z)$  for the redshift sample and corresponding random catalog. The solid line is  $\frac{dN}{dz}$  for the redshift sample; the distribution of the random catalog is indicated by the dotted line. The two vertical lines indicate the redshift range containing the 38 objects present in the redshift sample but not in the field sample. The random distribution has been normalized so as to have the same integral as the data distribution over the redshift range shown.

Fig. 3.— The angular correlation function  $w(\theta)$  for the photometric and redshift samples. The values of  $w$  for the photometric sample are indicated by dots; the data for the redshift sample are indicated by crosses. The error bars are the 68.3% uncertainties estimated from 300 bootstrap resamplings of the data. The solid line is given by the least-squares fit to the photometric data, with  $\delta$  in equation (9) fixed to 0.7.

Fig. 4.— The counts in excess of random within a cylinder of radius  $1 h^{-1}\text{Mpc}$  and length  $2\pi$ ,  $2\pi\bar{n} J_p(1 h^{-1}\text{Mpc}, \pi)$ , for the field sample, for  $\Omega_0 = 1$  and 0.2. The error bars are the 68.3% bootstrap confidence intervals.

Fig. 5.— The projected correlation function  $w_p(r_p)$  for the field sample, for  $\Omega_0 = 1$  and 0.2. The error bars are the 68.3% bootstrap confidence intervals. The solid line in each panel is from the least-squares fit of equation (17) to the data with  $\delta$  fixed to 0.7.

Fig. 6.— The redshift space correlation function  $\xi(s)$  for the field sample, for  $\Omega_0 = 1$  and 0.2. The error bars are the 68.3% bootstrap confidence intervals. The dashed line in each panel is the a power-law with  $\gamma = 1.7$  and  $r_0$  taken from the fit to the corresponding projected correlation function data. The solid curve in each panel is given by equation (23), with  $\sigma = 770 \text{ km s}^{-1}$  ( $\Omega_0 = 1$ ) and  $400 \text{ km s}^{-1}$  ( $\Omega_0 = 0.2$ ). The dotted curve is obtained using a Gaussian with  $\sigma = 140 \text{ km s}^{-1}$  in place of the exponential in the velocity distribution model (24).

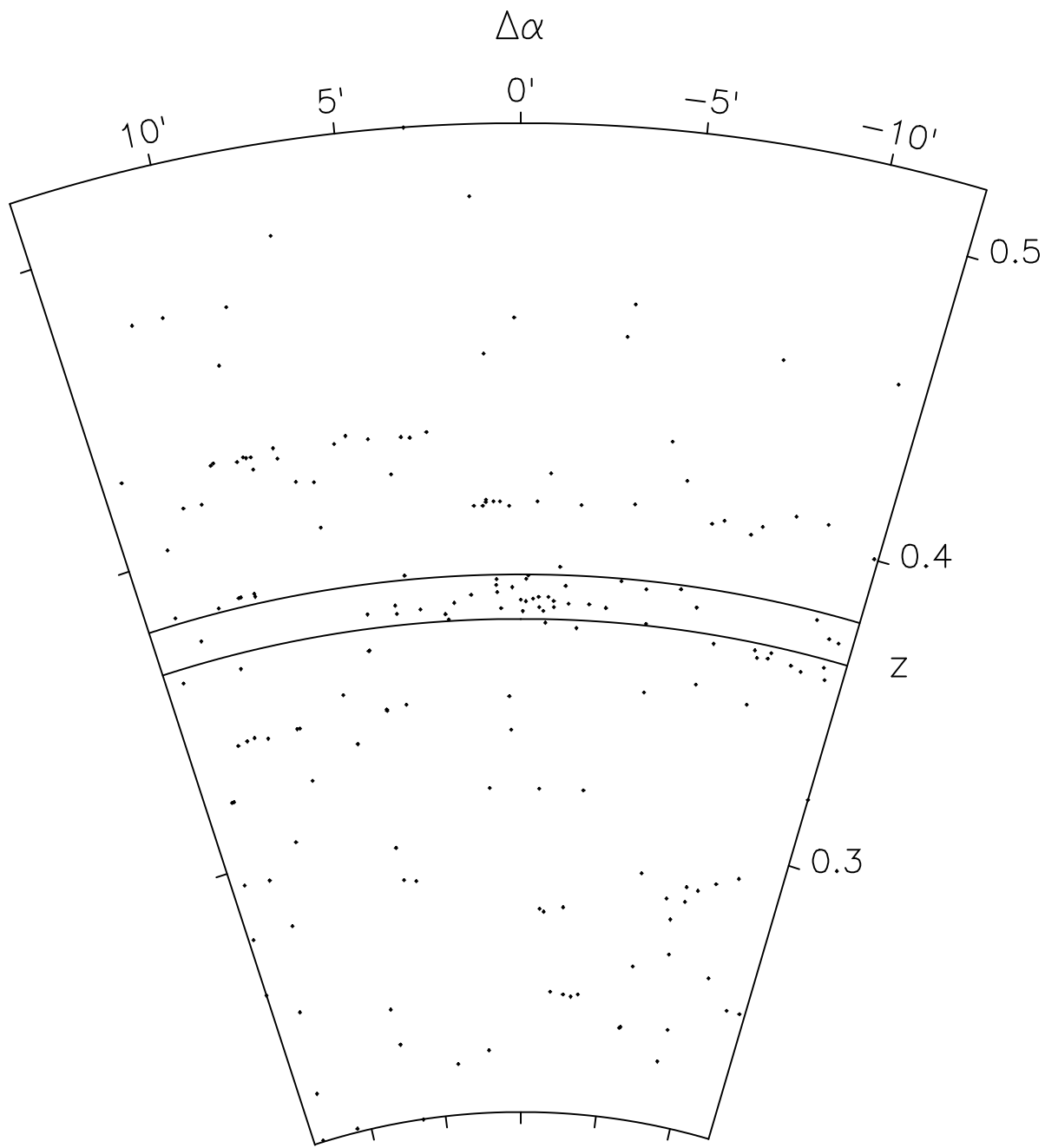


Fig. 1.—

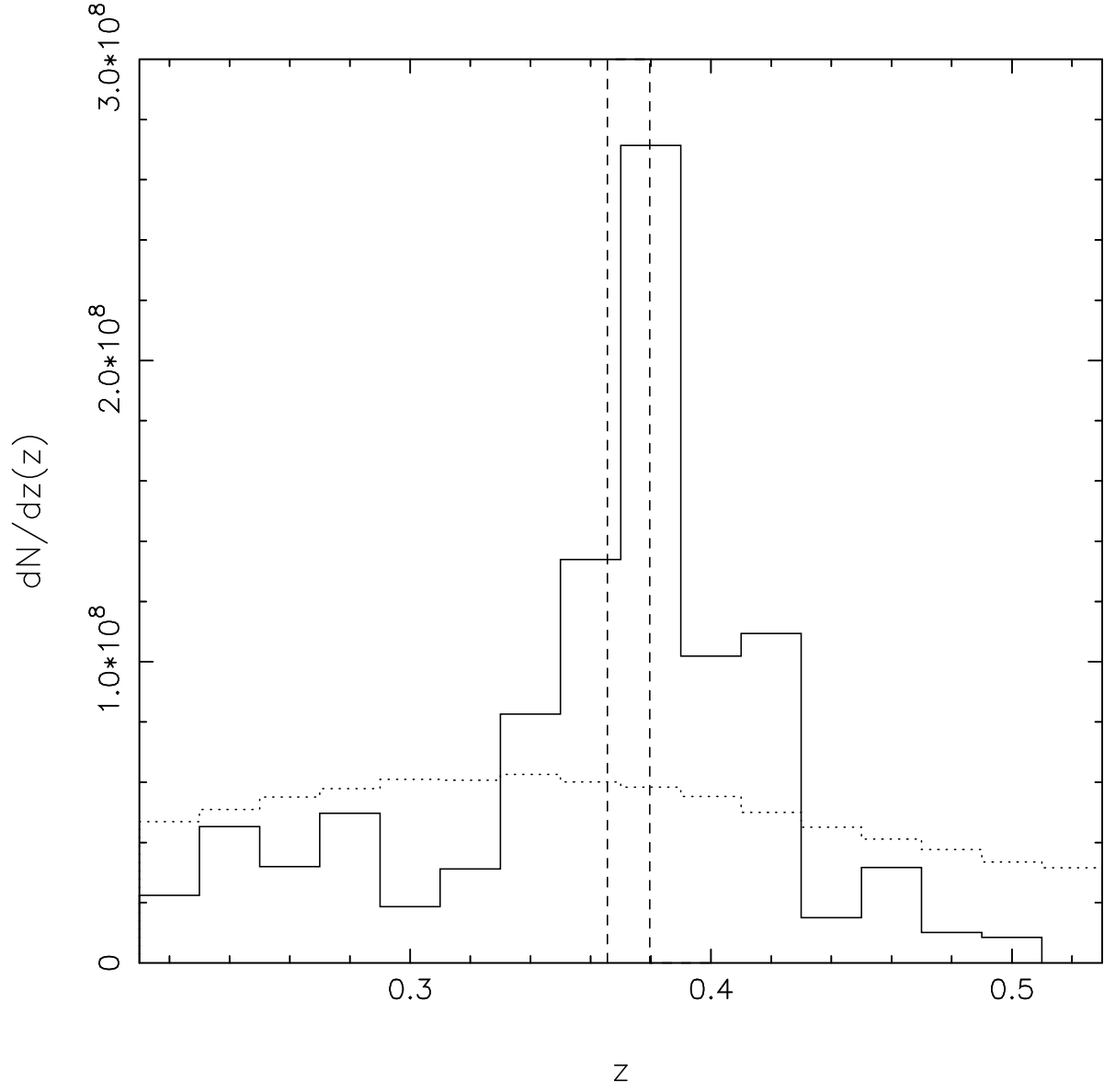


Fig. 2.—

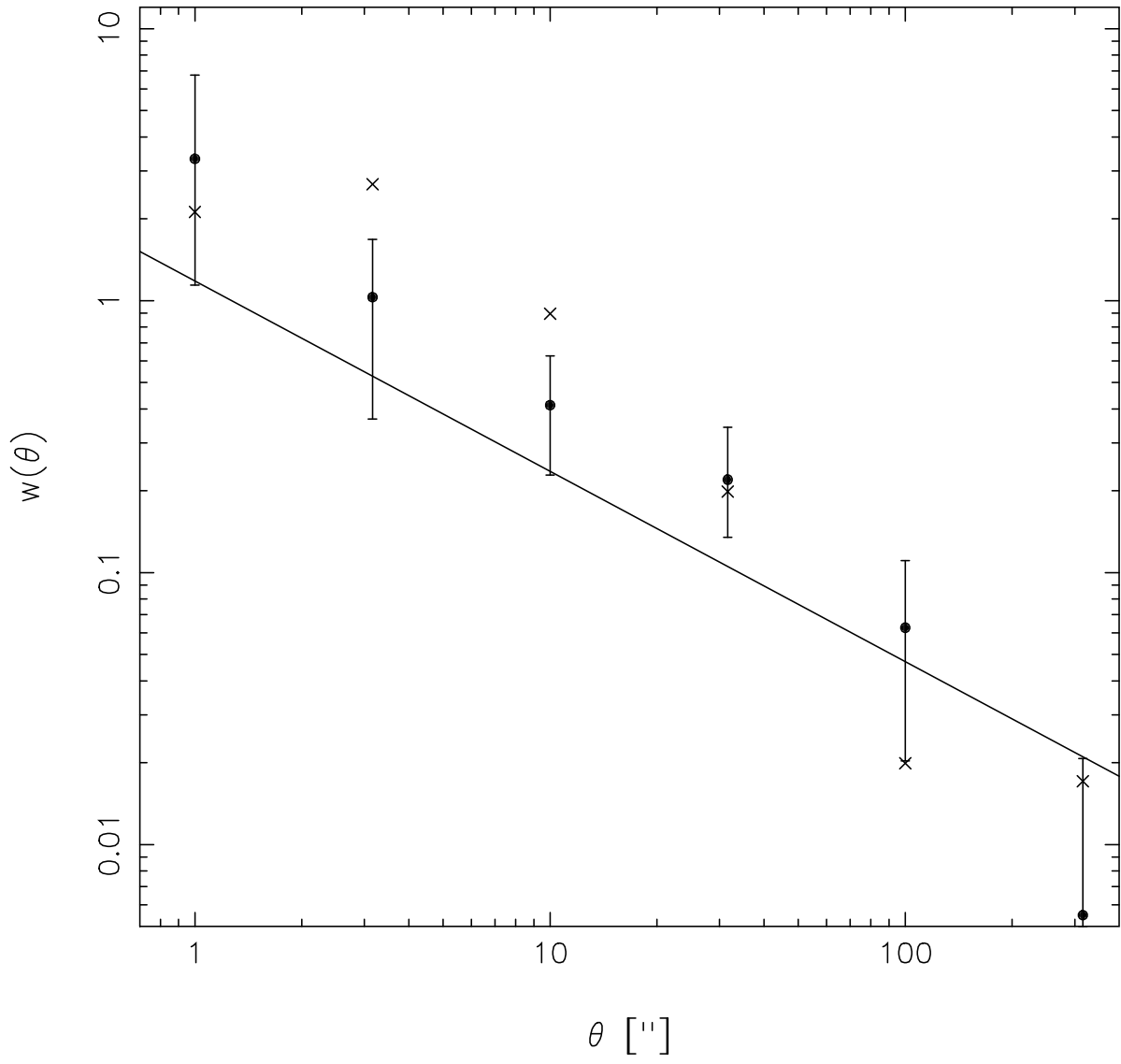


Fig. 3.—

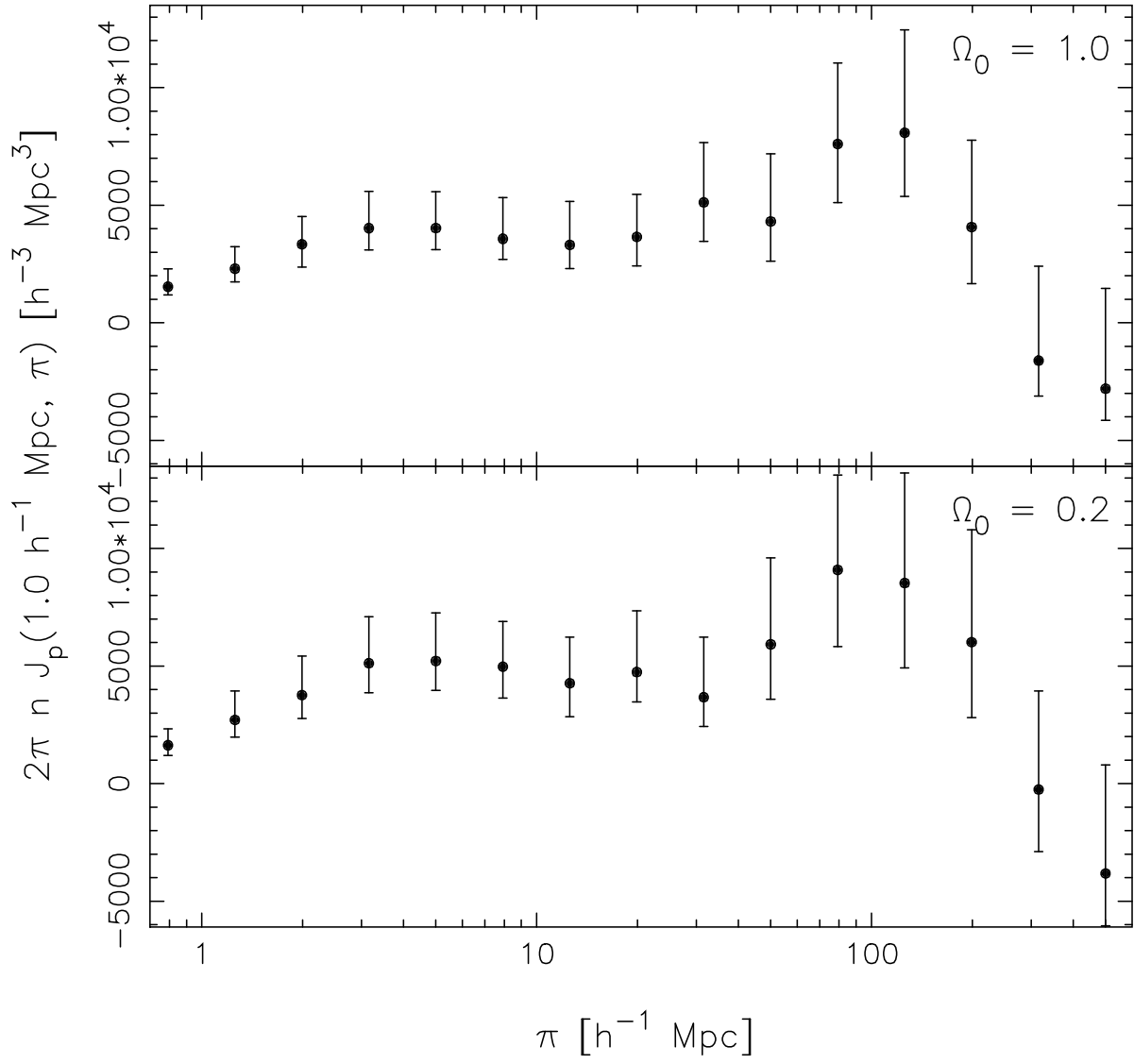


Fig. 4.—

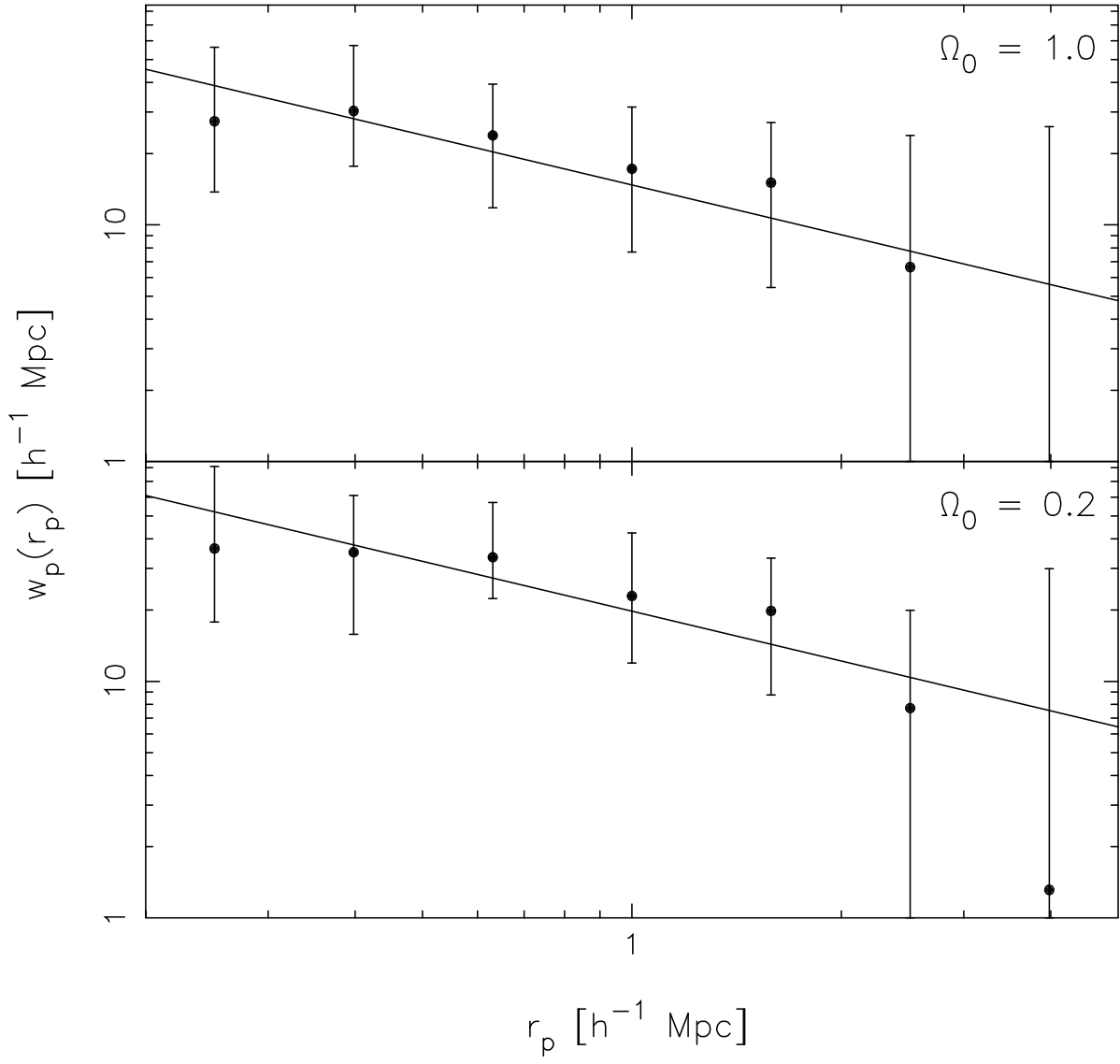


Fig. 5.—

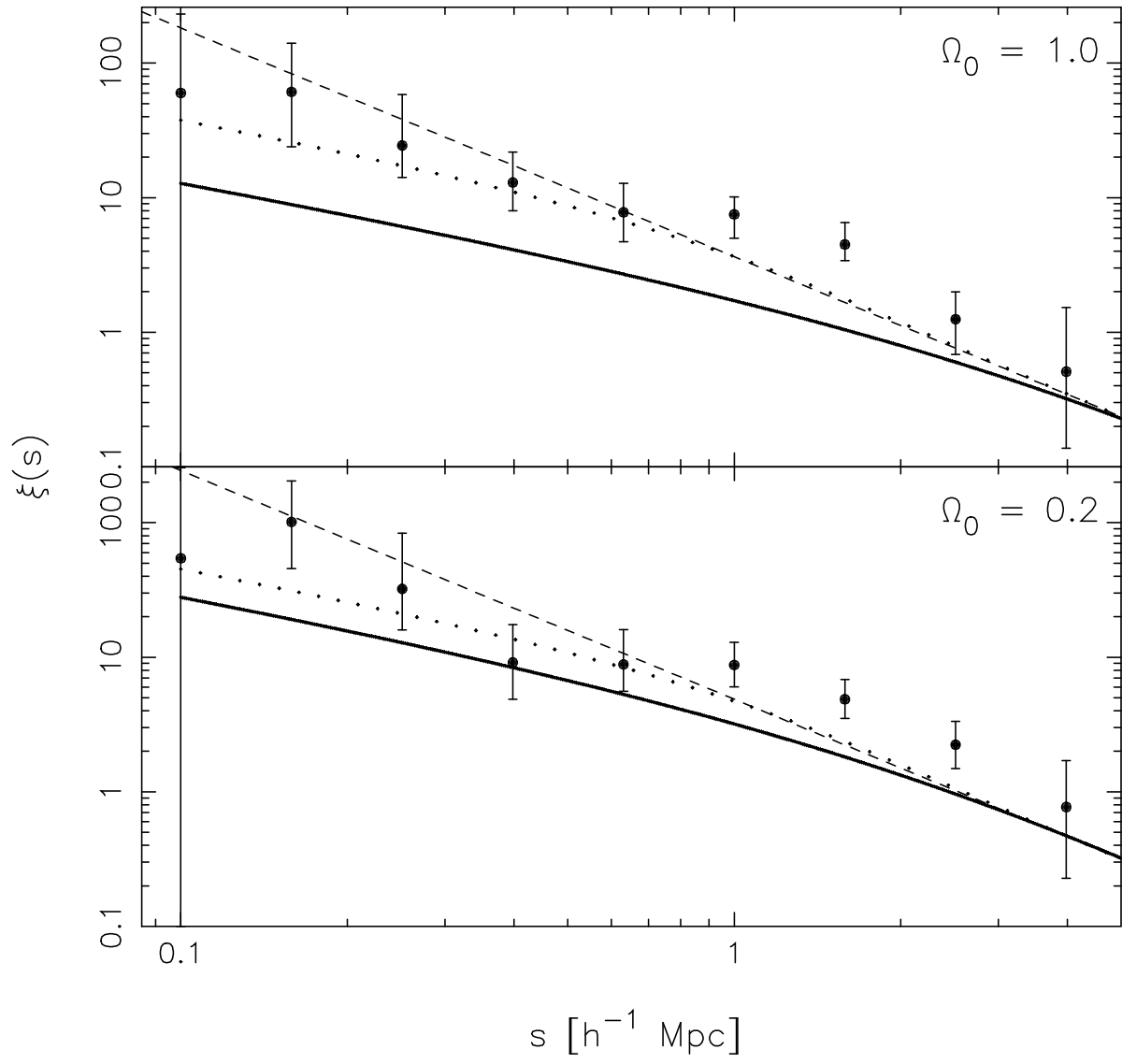


Fig. 6.—